

On the Reynolds-number scaling of Poisson solver complexity

F.X.Trias,^{1, a)} A.Alsalti-Baldellou,^{1, 2, b)} and A.Oliva^{1, c)}

¹⁾*Heat and Mass Transfer Technological Center, Technical University of Catalonia, c/Colom 11, 08222 Terrassa (Barcelona), Spain*

²⁾*Department ICEA, University of Padova, Via Francesco Marzolo, 9, 35131 Padova PD, Italy*

(Dated: 30 December 2025)

We aim to answer the following question: *is the complexity of numerically solving Poisson's equation increasing or decreasing for very large simulations of incompressible flows?* Physical and numerical arguments are combined to derive power-law scalings at very high Reynolds numbers. A theoretical convergence analysis for both Jacobi and multigrid solvers defines a two-dimensional phase space divided into two regions depending on whether the number of solver iterations tends to decrease or increase with the Reynolds number. Numerical results indicate that, for Navier–Stokes turbulence, the complexity decreases with increasing Reynolds number, whereas for the one-dimensional Burgers' equation it follows the opposite trend. The proposed theoretical framework thus provides a unified perspective on how solver convergence scales with *Re*-number and offers valuable guidance for the development of next-generation preconditioning and multigrid strategies for extreme-scale simulations.

^{a)}francesc.xavier.trias@upc.edu

^{b)}adel.alsaltibaldellou@unipd.it

^{c)}asensio.oliva@upc.edu

I. INTRODUCTION

We consider the direct numerical simulation (DNS) of turbulent incompressible flows. For clarity in the forthcoming analysis, we restrict attention to Newtonian fluids with constant physical properties. This assumption does not entail any loss of generality for the arguments developed here. Under these assumptions, the governing Navier–Stokes (NS) equations in non-dimensional form read

$$\partial_t \mathbf{u} + (\mathbf{u} \cdot \nabla) \mathbf{u} = \frac{1}{Re} \nabla^2 \mathbf{u} - \nabla p, \quad \nabla \cdot \mathbf{u} = 0, \quad (1)$$

where $\mathbf{u}(\mathbf{x}, t)$ and $p(\mathbf{x}, t)$ denote the velocity and pressure fields, respectively, and $Re = Ul/\nu$ is the Reynolds number. Here, ν is the kinematic viscosity, while U and l denote the characteristic velocity and length scale, respectively, which are typically associated with the motion of the largest flow scales.

Then, these equations must be discretized in both space and time. For the spatial discretization, a wide variety of numerical methods and schemes are available¹. Their choice depends on factors such as local accuracy, numerical stability, boundedness, and the conservation of global quantities such as momentum and kinetic energy, among others. The earliest DNS studies of turbulent flows were restricted to simple configurations, primarily homogeneous isotropic turbulence (HIT) simulations^{2–4} and turbulent channel flows^{5,6} at moderate Re -numbers. These simulations relied on Fourier (or Fourier–Chebyshev for channel flows) pseudospectral methods, combined with dealiasing techniques to treat the nonlinear convective terms⁷. Over the past decades, advances in numerical algorithms and high-performance computing (HPC) systems enabled DNS at higher Re -numbers^{8–14} and more complex flow configurations^{15–23}. In parallel, community-accessible resources such as the Johns Hopkins Turbulence Database^{24,25} have provided researchers with unprecedented access to large-scale DNS datasets, including homogeneous isotropic turbulence up to $Re_\lambda \approx 2500$ at 32768^3 resolution, as well as other canonical flows. While Fourier-based methods remain the standard for canonical configurations, mesh-based approaches such as finite-volume, finite-difference, and finite-element methods have become essential to simulate turbulence in complex geometries. From a physical perspective, turbulence arises from the intricate interplay between nonlinear convection, which transfers kinetic energy from large to small scales, and viscous dissipation, which ultimately balances this transfer. Numerically, schemes that introduce

artificial dissipation can severely distort this balance at the smallest scales. Consequently, it is widely accepted within the DNS community that, regardless of the discretization method, reliable simulations require numerical methods that are virtually free from artificial dissipation^{26–32}.

In addition to spatial discretization, the governing equations must be advanced in time, which requires addressing both the integration of the momentum equations and the pressure–velocity coupling inherent to incompressible flows. Starting from the pioneering simulations of HIT and channel flows, most DNS simulations of incompressible turbulence have been performed using fractional-step projection methods³³ combined with either explicit or semi-implicit time integration for the momentum equation. In virtually all cases, the non-linear convective term is treated explicitly, which severely restricts the allowable time-step. Specifically, the eigenvalues of the linearized system, scaled by the chosen time-step, must remain within the stability region of the temporal scheme³⁴. This restriction is usually expressed through the CFL condition³⁵. Consequently, each time-step requires the solution of a pressure Poisson equation, which usually represents the dominant computational cost and the main bottleneck in large-scale DNS of incompressible flows.

One of the most efficient approaches to solve such a Poisson equation is through iterative methods based on Krylov subspaces³⁶, whose implementation is simple and easily parallelisable, requiring only basic linear algebra operations. However, iterative linear solvers must be properly preconditioned to be effective³⁷. In this sense, while preconditioners based on incomplete factorizations were very popular in the early days of numerical linear algebra³⁸, their sequential nature and the increasing availability of parallel computers made them lose ground against alternatives with higher degrees of parallelism, such as sparse approximate inverses^{39,40}, whose application solely relies on the sparse-matrix vector product.

Regardless of their specific features, none of these methods are *optimal* in the sense that when augmenting the mesh resolution (hence increasing the linear system size), the problem becomes more ill-conditioned and more iterations are required to reach the same accuracy. This problem worsens nowadays, as cutting-edge DNS require solving extreme-scale linear systems on massively parallel supercomputers, and single-level preconditioners generally require excessive iterations.

The problem of weak scalability is overcome with multilevel preconditioners like geometric

or algebraic multigrid^{41,42} (MG). They combine the “smoothing” properties of single-level methods with the robustness of direct solvers by assembling a hierarchy of grids and taking advantage of the fact that smooth error becomes less smooth after coarsening. Then, a single-level preconditioner smooths the error at each level, and a direct solver removes the remaining low-frequency modes at the coarsest level. To ensure an effective interplay between smoother and coarse-grid correction, the transfer operators used to jump between levels (restriction and prolongation) must preserve the near-null space of the coefficient matrix. When done accurately, MG preconditioners provide convergence rates independent (or mildly dependent) of the grid size and, owing to their parallel efficiency, often exhibit an almost ideal weak scaling.

In summary, reliable numerical techniques for DNS of incompressible flows in complex geometries are well established. This includes both advanced spatial discretizations, accurate time-integration methods and advanced Poisson solvers. Nevertheless, the achievable *Re*-numbers remain constrained by the computational capacity of modern HPC systems. With the continuous growth of computational power, it is reasonable to anticipate DNS at progressively higher *Re* in the coming decades. This raises a fundamental question: *as the Re-number increases, will the relative cost of solving the pressure Poisson equation decrease, remain constant, or instead become an even more critical bottleneck?*

To answer this question, both physical and numerical arguments are combined in the next sections. Firstly, we analyze the spectral distribution of the Poisson solver residual. We identify the two main competing effects and how the spectral distribution of the residual scales with the *Re*-number. Then, in Section III, we use these findings to study whether the number of iterations inside the Poisson’s solver increases or decreases with *Re*. The theoretical predictions are validated in Section IV through numerical experiments for both the incompressible NS equations and the 1D Burgers’ equation. Test cases for the NS equations include HIT, air-filled Rayleigh–Bénard convection at different Rayleigh numbers, and flow around a square cylinder at different *Re*-numbers. On the other hand, the Burgers’ equation tests cover a very wide range of *Re* allowing a verification of the proposed scaling laws. Finally, relevant results are summarized and conclusions are given.

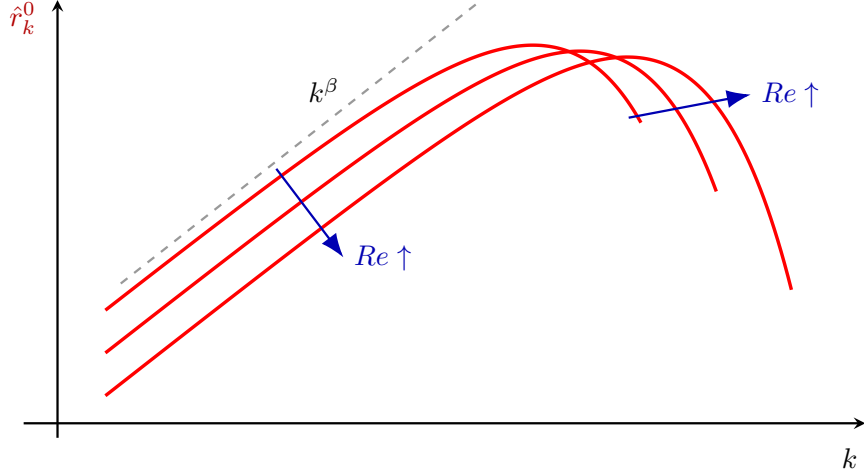


FIG. 1. Illustrative explanation of the two competing effects on the solution of Poisson's equation when increasing Re number: time-step, Δt , decreases leading to smaller values of the initial residual, \hat{r}_k^0 , whereas the range of scales increases.

II. ANALYSIS OF THE RESIDUAL OF POISSON'S EQUATION

A. Two competing effects

The steadily increasing capacity of modern HPC systems enables DNS at higher and higher Reynolds numbers, $Re = Ul/\nu$, where U and l denote the characteristic velocity and length scale of the largest flow structures. The computational requirements, in terms of the number of grid points in each direction, N_x , and time-steps, N_t , can be estimated from the classical Kolmogorov theory⁴³ (K41):

$$N_x^{K41} = \frac{L_x}{\Delta x} \sim \frac{l}{\eta} \sim Re^{3/4}, \quad (2)$$

$$N_t^{K41} = \frac{t_{\text{sim}}}{\Delta t} \sim \frac{t_l}{t_\eta} \sim \frac{l}{\eta} \frac{u}{U} \sim Re^{3/4} Re^{-1/4} = Re^{1/2}, \quad (3)$$

where L_x and t_{sim} are the domain size and total simulation time, assumed to scale with the largest turbulent structures, *i.e.* $L_x \sim l$ and $t_{\text{sim}} \sim t_l$, with $t_l \sim l/U$. For DNS resolution, one requires $\Delta x \sim \eta$ and $\Delta t \sim t_\eta \sim \eta/u$, where η and u denote the Kolmogorov length and velocity scales, respectively.

Applying the CFL stability constraints^{34,35},

$$\Delta t^{\text{conv}} \sim \frac{\Delta x}{U} \quad \Delta t^{\text{diff}} \sim \frac{\Delta x^2}{\nu}, \quad (4)$$

to both the convective and diffusive terms, leads to the following estimation for the number of time-steps,

$$N_t^{\text{conv}} \sim \frac{t_l}{\Delta t^{\text{conv}}} \sim \frac{l}{U} \frac{U}{l Re^{-3/4}} = Re^{3/4}, \quad (5)$$

$$N_t^{\text{diff}} \sim \frac{t_l}{\Delta t^{\text{diff}}} \sim \frac{l}{U} \frac{\nu}{l^2 (Re^{-3/4})^2} = Re^{1/2}. \quad (6)$$

Hence, the normalized time-step scales as

$$\frac{\Delta t}{t_l} \sim \frac{1}{N_t} \sim Re^\alpha \quad \text{with} \quad \alpha = \begin{cases} -1/2 & \text{for K41 (Eq.3) or diffusion dominant (Eq.6)} \\ -3/4 & \text{for convection dominant as Eq.(5)} \end{cases} \quad (7)$$

In summary, increasing Re simultaneously requires (i) larger computational grids and (ii) smaller time-steps. These two effects act in opposite directions regarding the convergence of the pressure Poisson equation: larger meshes increase the condition number of the discrete Laplacian operator, while smaller time-steps improve the quality of the initial guess. The central question is thus: *which effect dominates at very high Re ?*

B. Reynolds number scaling of the solver residual

Although FFT-based direct solvers are very efficient for canonical flows with periodic directions^{44–46}, for extreme-scale simulations in complex geometries MG methods are expected to be the method of choice. Their fast convergence results from the complementary roles played by the smoother, which is responsible for damping high-frequency error components, and the coarse-grid correction, which in turn reduces low-frequency modes. We therefore analyze the residual of the Poisson equation as a function of the Re -number, focusing on two key aspects: its magnitude and its spectral distribution. To study them, we consider a fractional step method³³ where \mathbf{u}^p is the predictor velocity. Imposing that $\nabla \cdot \mathbf{u}^{n+1} = 0$, leads to a Poisson equation for the pressure field, p^{n+1} ,

$$\mathbf{u}^{n+1} = \mathbf{u}^p - \Delta t \nabla p^{n+1} \quad \xrightarrow{\nabla \cdot} \quad \nabla^2 p^{n+1} = \frac{1}{\Delta t} \nabla \cdot \mathbf{u}^p. \quad (8)$$

Assuming a constant time step Δt , and taking p^n as the initial guess, the initial residual becomes

$$r^0 = \nabla^2 p^n - \frac{1}{\Delta t} \nabla \cdot \mathbf{u}^{p,n+1} \stackrel{(8)}{=} \frac{1}{\Delta t} (\nabla \cdot \mathbf{u}^{p,n} - \nabla \cdot \mathbf{u}^{p,n+1}) \approx \partial_t \nabla \cdot \mathbf{u}^p, \quad (9)$$

where $\mathbf{u}^{p,n}$ and $\mathbf{u}^{p,n+1}$ denote the predictor velocities used to compute \mathbf{u}^n and \mathbf{u}^{n+1} , respectively. Note that we assume that the incompressibility constraint is satisfied at the previous time-step, *i.e.* $\nabla \cdot \mathbf{u}^n = 0$. In practice, this condition is satisfied only up to the user-prescribed residual of the Poisson solver, *i.e.* $|\nabla \cdot \mathbf{u}^n| \leq \epsilon$. Nevertheless, the following analysis remains valid provided that the absolute variation of the initial residual between consecutive time steps is much larger than this tolerance, *i.e.* $|r^{0,n+1} - r^{0,n}| \gg \epsilon$.

Alternatively, we can also consider $\tilde{r}^0 = \Delta t r^0$. In this case, the residual reads

$$\tilde{r}^0 = \nabla^2 \tilde{p}^n - \nabla \cdot \mathbf{u}^{p,n+1} \stackrel{(8)}{=} (\nabla \cdot \mathbf{u}^{p,n} - \nabla \cdot \mathbf{u}^{p,n+1}) \approx \Delta t \partial_t \nabla \cdot \mathbf{u}^p, \quad (10)$$

where $\tilde{p} = p \Delta t$ is a pseudo-pressure, *i.e.* pressure re-scaled by Δt . Notice that the scaled residual, \tilde{r}^0 , is physically more meaningful, as it directly measures the accuracy with which the incompressibility constraint is imposed. Unless otherwise stated, the superscript in the residual denotes the iteration number within the Poisson solver.

Then, recalling that $\nabla \cdot \mathbf{u}^p$ can be expressed as follows (see, for instance, Batchelor⁴⁷ or the textbook treatment in Chapter 2 of Pope⁴⁸)

$$\nabla \cdot \mathbf{u}^p \approx \Delta t \nabla \cdot (\mathbf{u} \cdot \nabla \mathbf{u}) = 2 \Delta t Q_G, \quad (11)$$

leads to

$$r^0 \approx 2 \Delta t^q \partial_t Q_G \quad \text{with} \quad q = \begin{cases} 1 & \text{if } r^0 \text{ defined as in Eq.(9)} \\ 2 & \text{if } r^0 \text{ defined as in Eq.(10)} \end{cases} \quad (12)$$

where $Q_G = -1/2 \text{tr}(\mathbf{G}^2)$ is the second invariant of the velocity gradient tensor, $\mathbf{G} \equiv \nabla \mathbf{u}$. Hence, smaller Δt reduces both r^0 and \tilde{r}^0 , leading to faster convergence.

At the same time, increasing Re implies finer grids (Eq. 2), resulting in a broader range of scales and, consequently, a more ill-conditioned Poisson equation. Therefore, the spectral distribution of the residual \hat{r}_k^0 is of central importance. Assuming a power-law scaling in the inertial range with slope β , we obtain,

$$\partial_t (\hat{Q}_G)_k \propto k^\beta \quad \Rightarrow \quad \hat{r}_k^0 \stackrel{(12)}{\approx} 2 \Delta t^q \partial_t (\hat{Q}_G)_k \propto \Delta t^q k^\beta, \quad (13)$$

where k is the wavenumber and $q \in \{1, 2\}$ depends on the definition of the residual: $q = 1$ for Eq. (9) and $q = 2$ for Eq. (10). This power-law scaling is confirmed *a posteriori* by the numerical results presented in Section IV.

A power-law scaling for Q_{G} can be derived from Eqs.(8) and (11), and the $k^{-7/3}$ scaling of the shell-summed squared pressure spectrum^{3,4,47,49–52},

$$(\hat{Q}_{\mathsf{G}})_k \propto k^2 (k^{-7/3})^{1/2} = k^{5/6}. \quad (14)$$

Then, the exponent value β in Eq.(13) can be inferred from the dynamics of the invariants obtained from the so-called restricted Euler equation⁵³,

$$\partial_t Q_{\mathsf{G}} = -(\mathbf{u} \cdot \nabla) Q_{\mathsf{G}} - 3R_{\mathsf{G}}, \quad (15)$$

where $R_{\mathsf{G}} = \det(\mathsf{G}) = 1/3\text{tr}(\mathsf{G}^3)$ is the third invariant of G . The two terms on the right-hand side scale differently. Specifically,

$$((\widehat{\mathbf{u} \cdot \nabla} Q_{\mathsf{G}})_k \propto (\widehat{\nabla Q_{\mathsf{G}}})_k \propto k(k^{5/6}) = k^{11/6}, \quad (16)$$

$$(\hat{R}_{\mathsf{G}})_k \propto (k^{5/6})^{3/2} = k^{5/4}, \quad (17)$$

where Taylor's frozen-turbulence hypothesis⁵⁴ is applied to approximate the convective term, $(\mathbf{u} \cdot \nabla) Q_{\mathsf{G}}$, which is expected to become the dominant contribution on the right-hand side of Eq.(15) due to its steeper k -scaling. Combining this with the results obtained in Eqs.(13) and (16) leads to

$$\hat{r}_k^0 \propto \Delta t^q k^\beta \quad \text{with} \quad \beta = 11/6. \quad (18)$$

Furthermore, we can assume that, given a flow configuration, the proportionality constant, C_r , scales with the inverse of the Re -number

$$\hat{r}_k^0 \approx C_r(Re) \Delta t^q k^\beta \propto Re^{-1} \Delta t^q k^\beta \quad \text{with} \quad \beta = 11/6. \quad (19)$$

The reasoning behind this scaling is the following. Let us consider a flow configuration with a forcing term that keeps the energy of the largest scales constant, independently of the Re -number. If we also assume that the flow is in equilibrium, *i.e.* the energy distribution remains approximately constant over time, then the non-linear convective term scales with the inverse of Re

$$(\widehat{\mathbf{u} \cdot \nabla \mathbf{u}})_k \sim \frac{k^2}{Re} \hat{\mathbf{u}}_k. \quad (20)$$

Plugging this into Eqs.(13) and (16) and recalling the definition of the invariant Q_{G} , given in Eq.(11), leads to the conclusion that $C_r(Re) \propto 1/Re$. Numerical tests with the 1D Burgers' equation, presented in Section IV C, confirm this scaling.

Then, combining the results obtained in Eqs.(12) and (19) leads to

$$\hat{r}_k^0 \propto Re^{-1} \Delta t^q k^\beta \quad \text{with} \quad \beta = 11/6 \quad \text{and} \quad q = \begin{cases} 1 & \text{if } \hat{r} \text{ defined as in Eq.(9)} \\ 2 & \text{if } \hat{r} \text{ defined as in Eq.(10)} \end{cases} \quad (21)$$

At this point, it is relevant to note that the derivation of this scaling relies on the classical $k^{-7/3}$ Kolmogorov scaling of the squared pressure spectrum in order to derive the scaling of the second invariant Q_G (see Eq. 14). This scaling is, in principle, expected to hold only in the bulk region of turbulent flows, where assumptions of local homogeneity and isotropy are approximately satisfied. In wall-bounded configurations, alternative scalings are predicted for the logarithmic layer, most notably a k^{-1} behavior arising from attached-eddy arguments⁵⁵, that has been reported in both experimental measurements⁵⁶ and numerical simulations^{14,52,57} of near-wall pressure fluctuations. Such deviations from the pressure scaling in the bulk region suggest that the dynamics of the invariant Q_G may differ in the near-wall region, as supported by studies reporting relevant changes in the invariant-based analysis of the flow topology in the near-wall region^{58,59}. This, in turn, may potentially lead to a modified value of the exponent β and, consequently, to different scaling trends for the Poisson solver residual. Nevertheless, the numerical results for wall-bounded turbulent flows presented in Section IV B support the idea that the effective value of β remains practically unchanged when compared to bulk turbulence. This behavior may be attributed to the inherently non-local nature of the pressure Poisson equation, which involves long-range interactions between outer-layer motions and the near-wall region that are not directly damped by viscosity¹⁴.

In summary, there are two competing effects (see Figure 1) when increasing the Re number: the time-step, Δt , and the proportionality constant decrease whereas the range of scales increases. The next step is to analyze how the solver convergence is affected.

III. ANALYSIS OF THE SOLVER CONVERGENCE

We want to study whether the number of iterations inside the Poisson's solver increases or decreases with Re . To do so, we can relate the L2-norm of the residual with the integral of \hat{r}_k^2 for all the wavenumbers using the Parseval's theorem, *i.e.*

$$\|r\|^2 = \int_{\Omega} r^2 dV = \int_1^{k_{\max}} \hat{r}_k^2 dk, \quad (22)$$

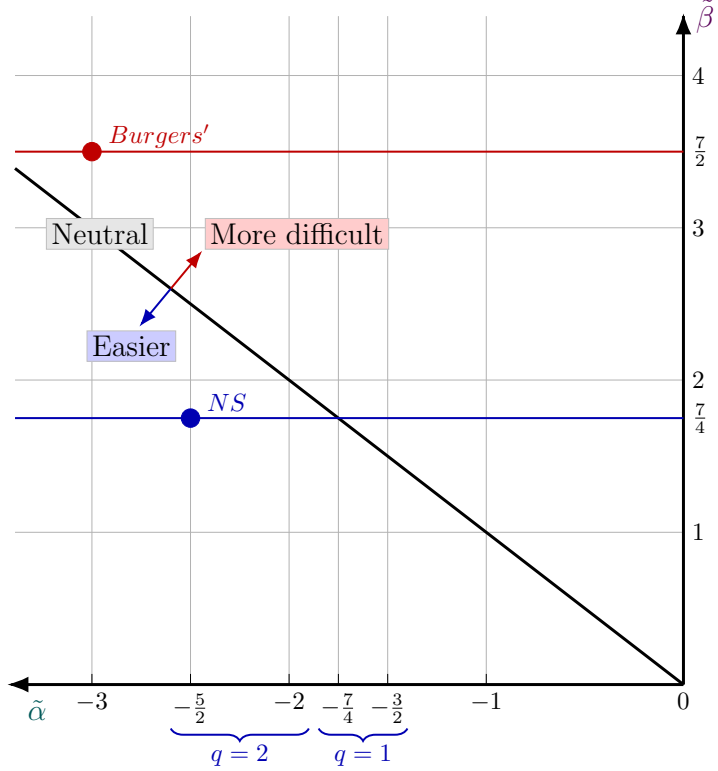


FIG. 2. Phase space $\{\tilde{\alpha}, \tilde{\beta}\}$. Solid black line corresponds to $\|r^n\|^2 \propto Re^0$ in Eqs.(31) and (39), *i.e.* neutral effect of Re -number in the total number of iterations, and corresponds to $\tilde{\alpha} = -\tilde{\beta}$. Horizontal blue line corresponds to $\tilde{\beta} = 7/4$ which is the estimation for the NS equations. The blue dot labeled as NS corresponds to the most common situation where $q = 2$ (see Eq. 12) and $\alpha = -3/4$ (see Eq. 7) leading to $\tilde{\alpha} = -5/2$ (see Eq. 25). The horizontal red line corresponds to the same analysis but for the Burgers' equation studied in Section IV.

where $k_{\max} \sim 1/\eta$ is the maximum wavenumber and η is the smallest resolved scale. Therefore, a power-law relation exists between k_{\max} and the Reynolds number,

$$k_{\max} \approx C_k Re^\gamma, \quad (23)$$

where, for the NS equations, the exponent is $\gamma = 3/4$ (see Eq. 2). Nevertheless, we retain the general form given in Eq. (23), since the Burgers' equation, characterized by a different value of γ (see Table I), is also examined numerically in the next section.

Then, the residual after n iterations can be computed as

$$\|r^n\|^2 = \int_1^{k_{\max}} (\hat{\omega}_k^n \hat{r}_k^0)^2 dk \stackrel{(7)(21)(23)}{\approx} \int_1^{C_k Re^\gamma} \hat{\omega}_k^{2n} Re^{2\tilde{\alpha}} k^{2\tilde{\beta}} dk, \quad (24)$$

where

$$\tilde{\alpha} \equiv q\alpha - 1, \quad (25)$$

and $\hat{\omega}_k = \hat{r}_k^{n+1}/\hat{r}_k^n$ is the convergence ratio of the solver. For instance, for a Jacobi solver, $\hat{\omega}_k = \cos(\frac{\pi}{2}\rho)$ where $\rho \equiv k/k_{\max}$, which corresponds to the classical second-order finite-difference (also finite-volume) discretization of the Poisson equation on a uniform grid⁶⁰; other discretizations lead to different expressions but exhibit the same qualitative behavior. In this case, using a quadratic approximation of $\cos(x) \approx 1 - 4x^2/\pi^2$ and applying the change of variable $k = k_{\max}\rho \approx C_k Re^\gamma \rho$ (see Eq. 23) leads to

$$\|r^n\|^2 \approx C_k^{2\beta+1} Re^{2(\tilde{\alpha}+\tilde{\beta})} \int_{1/k_{\max}}^1 \rho^{2\beta} (1 - \rho^2)^{2n} d\rho, \quad (26)$$

where

$$\tilde{\beta} \equiv \gamma \left(\beta + \frac{1}{2} \right). \quad (27)$$

Therefore, $\tilde{\alpha}$ in Eq.(25) represents the part of the residual that scales with Re that is associated with numerical aspects, whereas $\tilde{\beta}$ is determined by the underlying flow physics. For instance, in the case of the NS equations, $\gamma = 3/4$ (see Eq.2) and $\beta = 11/6$ (see Eq. 21), leading to $\tilde{\beta} = 7/4$.

Then, assuming that $k_{\max} \gg 1$, the integral can be accurately approximated by

$$\|r^n\|^2 \approx C_k^{2\beta+1} Re^{2(\tilde{\alpha}+\tilde{\beta})} \frac{1}{2} \mathcal{B}(\beta + 1/2, 2n + 1). \quad (28)$$

where $\mathcal{B}(a, b) = \int_0^1 t^{a-1} (1-t)^{b-1} dt$ is the beta function. Finally, assuming that $n \gg 1$, the beta function can be approximated as follows

$$\|r^n\|^2 \approx C_k^{2\beta+1} Re^{2(\tilde{\alpha}+\tilde{\beta})} \frac{1}{2} \Gamma(\beta + 1/2) (2n + 1)^{-(\beta+1/2)}, \quad (29)$$

whereas for the initial residual, $n = 0$, it can be approximated as

$$\|r^0\|^2 \approx C_k^{2\beta+1} Re^{2(\tilde{\alpha}+\tilde{\beta})} \frac{1}{2} \frac{\Gamma(\beta + 1/2)}{\Gamma(\beta + 3/2)}, \quad (30)$$

where $\Gamma(\cdot)$ is the gamma function. In summary, the L2-norm of the residual scales with Re and converges exponentially

$$\|r^n\|^2 \propto \frac{Re^{2(\tilde{\alpha}+\tilde{\beta})}}{(2n + 1)^{\beta+1/2}}. \quad (31)$$

Furthermore, from the expression given in Eqs.(31), we can deduce how the total number of solver iterations, n , scales with the Re -number. Namely, $n \propto Re^\xi$

$$Re^{2(\tilde{\alpha} + \tilde{\beta})} \sim (2n + 1)^{\beta+1/2} \propto n^{\xi(\beta+1/2)} \implies \xi = \frac{2(\tilde{\alpha} + \tilde{\beta})}{\beta + 1/2}. \quad (32)$$

Theoretical results for this Re -scaling are shown in the last column of Table I for both the NS and the Burgers' equation. The latter case will be analyzed in detail in Section IV C.

A. Extension to multigrid

We can extend this analysis for an MG solver with $l_{\max} \sim \log_2 N_x \sim \gamma \log_2 Re$ levels (see Eq. 23) and the Jacobi as smoother at each level. We also assume that the mesh resolution becomes twice coarser at each level. Then, the $L2$ -norm of the initial residual is distributed as follows

$$\begin{aligned} ||r^0||^2 &= \int_{k_{\max}/2}^{k_{\max}} (\hat{r}_k^0)^2 dk + \int_{k_{\max}/4}^{k_{\max}/2} (\hat{r}_k^0)^2 dk + \cdots + \int_{k_{\max}/2^{l_{\max}+1}}^{k_{\max}/2^{l_{\max}}} (\hat{r}_k^0)^2 dk + \int_1^{k_{\max}/2^{l_{\max}+1}} (\hat{r}_k^0)^2 dk \\ &= R_0 = R_{0,1} + R_{1,2} + \cdots + R_{l_{\max}-1,l_{\max}} + R_{l_{\max}}, \end{aligned} \quad (33)$$

where

$$R_{l_1, l_2} \equiv \int_{k_{\max}/2^{l_2}}^{k_{\max}/2^{l_1}} (\hat{r}_k^0)^2 dk \quad \text{and} \quad R_l \equiv \int_1^{k_{\max}/2^l} (\hat{r}_k^0)^2 dk, \quad (34)$$

represent the part of the $L2$ -norm of the initial residual contained between the wavenumbers $k_{\max}/2^{l_2}$ and $k_{\max}/2^{l_1}$, and below the wavenumber $k_{\max}/2^l$, respectively. Moreover, for the initial level, $l = 0$, we can accurately approximate the effective damping, given in Eq.(28), of the residual as follows

$$||r^n||^2 \approx C_k^{2\beta+1} Re^{2(\tilde{\alpha} + \tilde{\beta})} \frac{1}{2} (1 - \mathcal{B}_{1/2}(\beta + 1/2, 2n + 1)), \quad (35)$$

where $\mathcal{B}_x(a, b) = \int_0^x t^{a-1} (1-t)^{b-1}$ is the incomplete beta function. Recalling that $\mathcal{B}_{1/2}(a, b) = (1 - \mathcal{B}_{1/2}(b, a))$, we can write the previous expression more compactly as

$$||r^n||^2 \approx C_k^{2\beta+1} Re^{2(\tilde{\alpha} + \tilde{\beta})} \frac{1}{2} (\mathcal{B}_{1/2}(2n + 1, \beta + 1/2)). \quad (36)$$

The underlying idea is that the Jacobi smoother effectively damps only the high-frequency components of the error. Consequently, its influence is evaluated over the range $k_{\max}/2 < k \leq k_{\max}$, while its impact at lower wavenumbers is deliberately neglected. Therefore, it is

	α	q	$\tilde{\alpha}$	β	γ	$\tilde{\beta}$	ξ
Formula	Eq.(7)	Eq.(12)	Eq.(25)	Eq.(21)	Eq.(23)	Eq.(27)	Eq.(32)
NS	$-3/4$	2	$-5/2$	$11/6$	$3/4$	$7/4$	$-9/14$
	$-3/4$	1	$-7/4$	$11/6$	$3/4$	$7/4$	0
Formula	Eq.(44)	Eq.(12)	Eq.(25)	Eq.(47)	Eq.(23)	Eq.(27)	Eq.(32)
Burgers'	-1	2	-3	3	1	$7/2$	$2/7$
	-1	1	-2	3	1	$7/2$	$6/7$

TABLE I. Exponents for all the relevant scalings for both the NS and the Burgers' equation.

only damping $R_{0,1}$. The same logic applies to all the subsequent MG levels up to $l_{\max} - 1$ leading to

$$\|r^n\|^2 \approx \left(\sum_{l=0}^{l_{\max}-1} R_{l,l+1} \right) \frac{1}{2} \mathcal{B}_{1/2}(2n+1, \beta + 1/2) + \frac{R_{l_{\max}}}{2} \mathcal{B}(2n+1, \beta + 1/2) \quad (37)$$

$$\stackrel{(33)}{=} \frac{R_0 - R_{l_{\max}}}{2} \mathcal{B}_{1/2}(2n+1, \beta + 1/2) + \frac{R_{l_{\max}}}{2} \mathcal{B}(2n+1, \beta + 1/2). \quad (38)$$

Notice that the last level, l_{\max} , is also solved using a Jacobi solver. In a practical MG implementation, this last level is usually solved with a direct solver or, at least, with a more efficient solver⁶¹.

Recalling the definition of the residual, given in Eq.(28), it leads to

$$\|r^n\|^2 \approx C_k^{2\beta+1} Re^{2(\tilde{\alpha}+\tilde{\beta})} \left\{ \left(1 - \frac{R_{l_{\max}}}{R_0} \right) \frac{\mathcal{B}_{1/2}(2n+1, \beta + 1/2)}{2} + \frac{R_{l_{\max}}}{R_0} \frac{\mathcal{B}(2n+1, \beta + 1/2)}{2} \right\}. \quad (39)$$

Compared to Eq.(28), MG is strongly accelerated by the term in brackets. Moreover, notice that if $l_{\max} = 0$, *i.e.* zero MG level, it collapses to the formula derived for the Jacobi-only solver. Nevertheless, the scaling with Re is the same; therefore, the regions defined in the $\{\tilde{\alpha}, \tilde{\beta}\}$ phase space remain unchanged (see Figure 2).

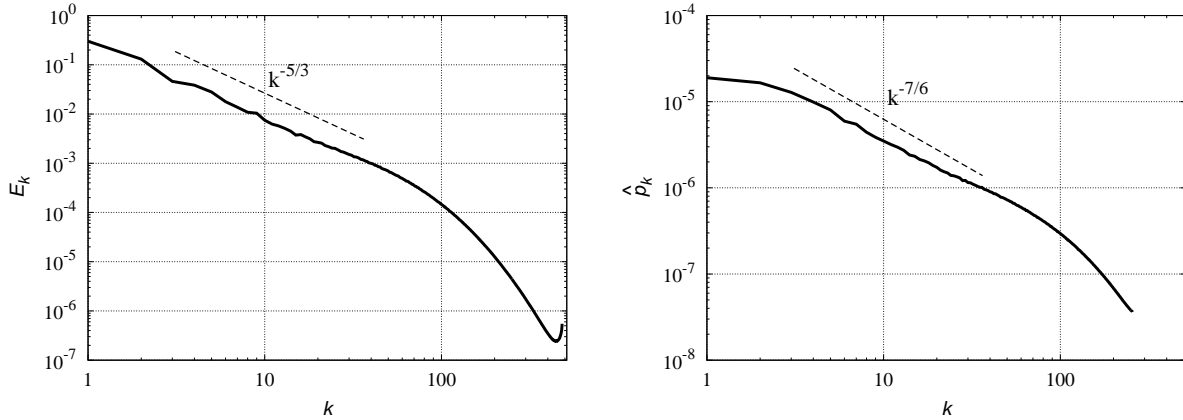


FIG. 3. Energy and pressure spectra for the forced HIT simulation at $Re_\lambda \approx 433$. Data has been obtained from the JHTDB database^{24,25}.

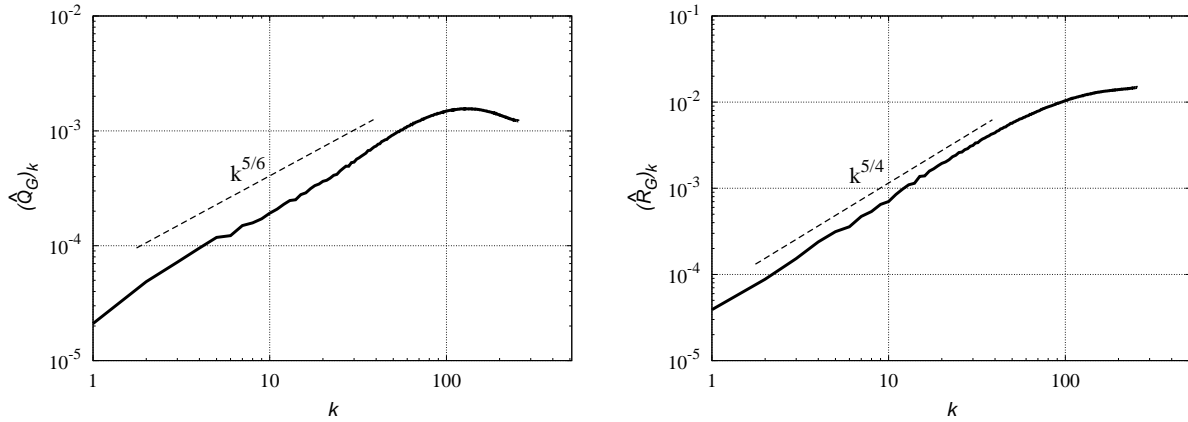


FIG. 4. Same as in Figure 3 but for the second, Q_G , and third invariant, R_G , of the velocity gradient tensor.

IV. NUMERICAL RESULTS

A. Homogeneous isotropic turbulence

As a first validation case, we consider the forced HIT using the data from the Johns Hopkins Turbulence Database (JHTDB)^{24,25}. The chosen dataset corresponds to a DNS of forced isotropic turbulence at Taylor microscale Reynolds number $Re_\lambda \approx 433$, carried out on a 1024^3 grid. The flow is statistically stationary due to a large-scale forcing that maintains a constant energy level in shells such that $k \leq 2$. The database provides access to velocity and pressure fields as well as all spatial derivatives over a sequence of consecutive time steps,

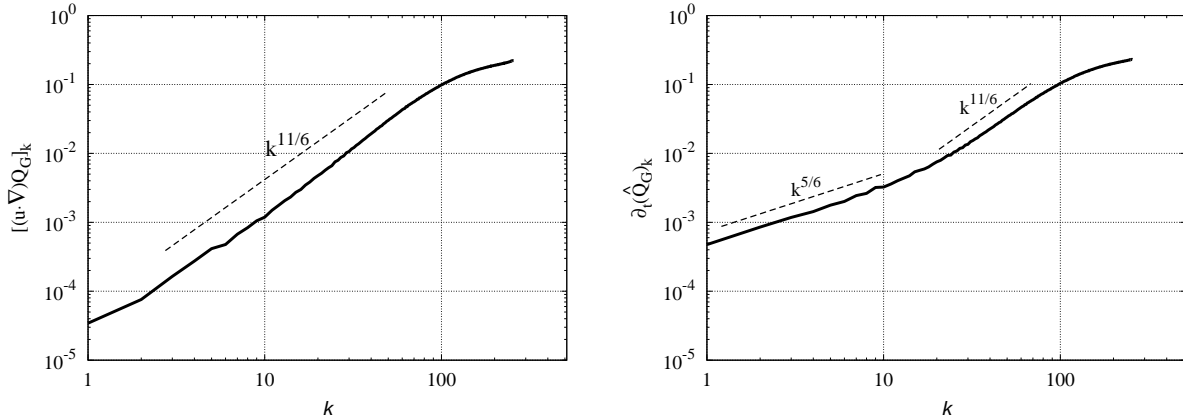


FIG. 5. Same as in Figure 3 but for the convective term, $(\mathbf{u} \cdot \nabla)Q_G$, and the residual of the Poisson equation.

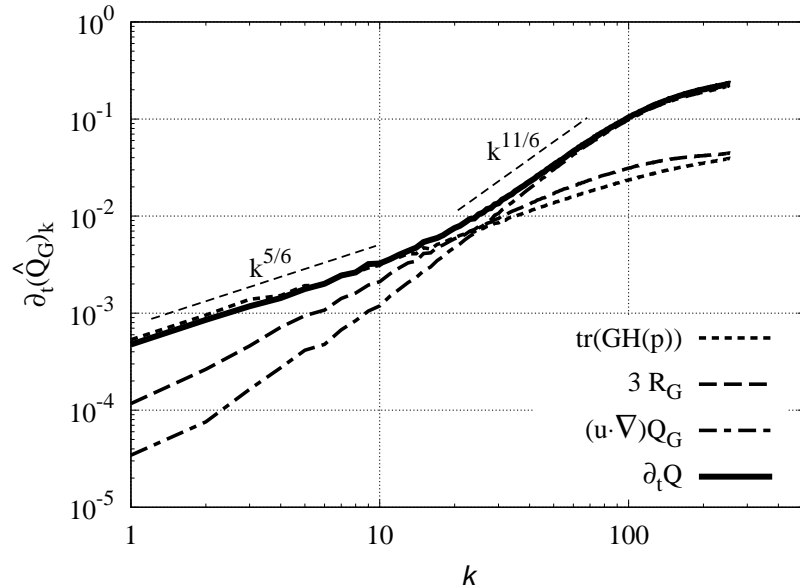


FIG. 6. Same as in Figure 3 but for $\partial_t Q_G$ and its breakdown into the different terms that contribute to it in Eq.(40).

which enables the computation of spectra of various quantities of interest, including the principal invariants of the velocity gradient tensor and their temporal derivatives. Further details regarding the numerical setup and simulation methodology can be found in the original publication⁶².

The homogeneous and isotropic nature of the flow makes this dataset an ideal benchmark for assessing the spectral scaling laws derived in Section II. As expected from the

classical turbulence theory, the kinetic energy spectrum reproduces the well-known Kolmogorov $k^{-5/3}$ scaling, while the pressure spectrum exhibits the $k^{-7/6}$ slope^{3,4,47,49–52}. These results, which are shown in Figure 3, are fully consistent with previous studies and confirm that the database accurately reproduces the universal features of isotropic turbulence across the inertial range. Then, the spectra for the second, Q_G , and third, R_G , principals invariants of the velocity gradient tensor are displayed in Figure 4. The power-law scalings are also consistent with the predictions given in Eqs.(14) and (17), respectively. This confirms the assumptions made in Section II B that eventually lead to the $\beta = 11/6$ scaling of the residual (see Eq. 21). This scaling follows from that of the convective term, $(\mathbf{u} \cdot \nabla)Q_G$, given in the Eq.(15), which is derived from the restricted Euler equation. The $k^{11/6}$ scaling of this term is confirmed in Figure 5 (left). Nevertheless, the spectrum of the $\partial_t Q_G$ shown in Figure 5 (right) shows two regions: namely, the predicted $11/6$ scaling at high wavenumbers, and a $5/6$ scaling at lower wavenumbers. This second scaling cannot be explained with the simplified model given in Eq.(15). Namely, the invariant R_G , which is the second term in the right-hand side of the equation, scales with $k^{5/4}$ as shown in Figure 4 (right) and may have relevance only at low wavenumbers. However, it does not explain the $5/6$ scaling observed in Figure 5 (right). To do so, we need a more complete model.

From the NS equations (1), we can derive all the terms that contribute to the evolution of the invariant Q_G ,

$$\partial_t Q_G = -(\mathbf{u} \cdot \nabla)Q_G - 3R_G + \text{tr}(\mathbf{G}H_p) - \frac{1}{Re} \text{tr}(\mathbf{G}\nabla^2\mathbf{G}), \quad (40)$$

where $H_p \equiv \nabla\nabla p$ is the Hessian of the pressure field. The last term represents the viscous effects, which are expected to have a relevant contribution only in the dissipation range but not in the inertial one. Therefore, we can restrict our analysis to the first three terms in the right-hand side of Eq.(40). Results are displayed in Figure 6. Firstly, we can confirm the dominance of the convective term $(\mathbf{u} \cdot \nabla)Q_G$ at high wavenumbers leading to the anticipated $11/6$ scaling. Secondly, we can now explain the $5/6$ scaling observed at low wavenumbers which is essencially due to the pressure effects through the term $\text{tr}(\mathbf{G}H_p)$ in Eq.(40).

In summary, the residual of the Poisson equation, r^0 , which is proportional to $\partial_t Q_G$ as shown in Eq.(12), has two relevant contributions: $(\mathbf{u} \cdot \nabla)Q_G$ and $\text{tr}(\mathbf{G}H_p)$, which correspond to the first and third term in the right-hand-side of Eq.(40), respectively. The latter scales with $k^{5/6}$ as shown in Figure 6 and is relevant only at low wavenumber, whereas the former scales

	S1	S2	S3	S4	S5	W1	W2	W3	W4
x	-0.45	-0.40	-0.30	0.00	0.50	1.00	1.50	2.50	3.50
y	0.63	0.63	0.63	0.63	0.63	0.00	0.00	0.00	0.00

TABLE II. List of monitoring locations for the square cylinder. The first five probes, labeled S1-S5, are located in the shear-layer region, while the remaining probes, labeled W1-W4, are located in the wake region.

	P1	P2	P3	P4	P5
x	1	2	1	2	3
y	0.5	0.5	0.5	0.5	0.5
z	0.001	0.001	0.5	0.5	0.5

TABLE III. List of monitoring locations for the Rayleigh–Bénard configuration. Probes P1 and P2 are located inside the boundary layer whereas probes P3 to P5 are in the bulk region.

with $k^{11/6}$ and eventually becomes the dominant at higher wavenumbers confirming the adequacy of the analysis done in Section II B. Nevertheless, two crucial issues remain to be demonstrated: (i) whether the proposed theory also applies to complex, non-homogeneous turbulent flows beyond HIT, and (ii) whether the predicted scalings of both the solver residual and the iteration count required to solve the Poisson equation are confirmed numerically. These two points are addressed in the next subsections.

B. Analysis of complex flows

In this subsection, we examine two non-homogeneous turbulent flow configurations: the flow around a square cylinder and an air-filled Rayleigh–Bénard convection (RBC). Both cases involve strongly inhomogeneous turbulence with a high degree of flow complexity. They correspond to configurations investigated in previous studies^{13,16} and are illustrated in Figure 7. Unlike HIT, the absence of homogeneity and isotropy in these flows prevents the computation of a fully three-dimensional spatial spectra, so alternative analysis must be employed. In this case, we can analyse the temporal evolution of the pressure field at different relevant locations. Namely, recalling the definition of the initial residual of the

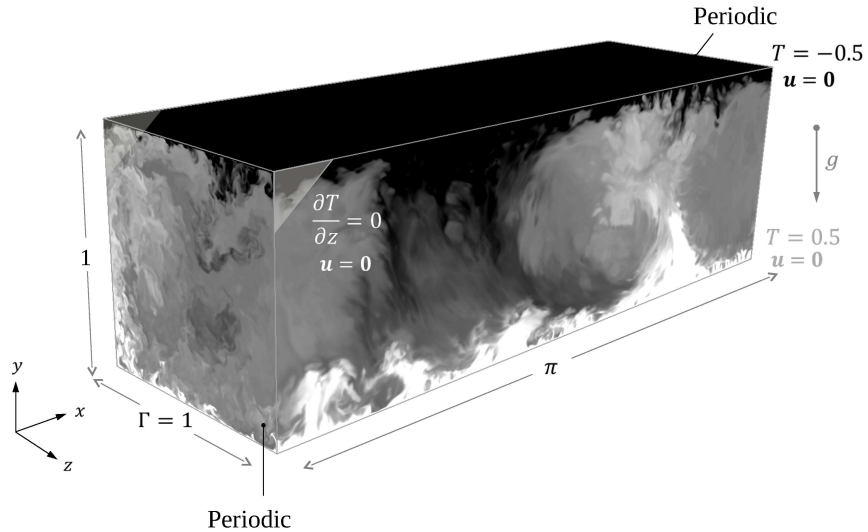
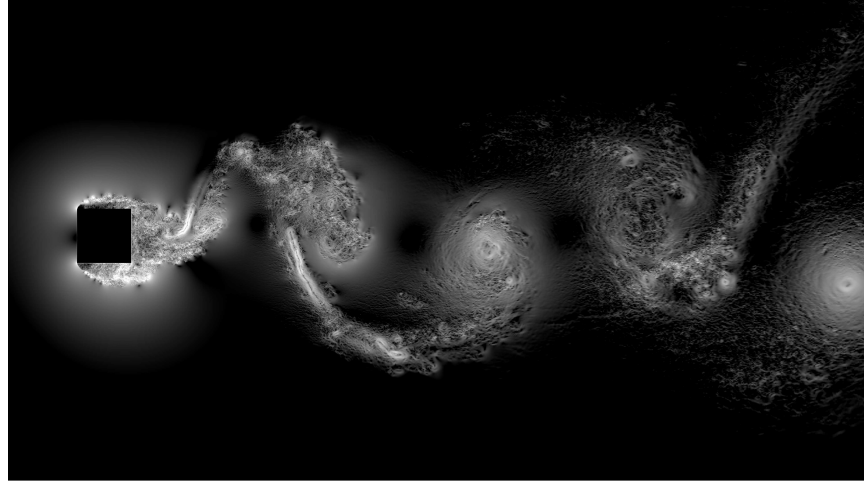


FIG. 7. Illustrative snapshots of the DNS simulations of complex non-homogeneous flows studied. Top: a turbulent flow around a square cylinder at $Re = 55000$ computed on 3136 CPU-cores of MareNostrum 5-GPP supercomputer with a mesh of 2.6 billion grid points. Bottom: an air-filled ($Pr = 0.7$) Rayleigh–Bénard configuration studied¹³ at Rayleigh numbers up to $Ra = 10^{11}$. The highest Ra was computed on 8192 CPU-cores of the MareNostrum 4 supercomputer using a mesh with 5.7 billion grid points.

Poisson solver, r^0 , given in Eqs.(9) and (12), we can relate the temporal derivatives of the pressure field and the invariant Q_G ,

$$\nabla^2 p^n - \nabla^2 p^{n+1} \approx 2\Delta t \partial_t Q_G \implies \nabla^2 \partial_t p \approx 2\partial_t Q_G. \quad (41)$$

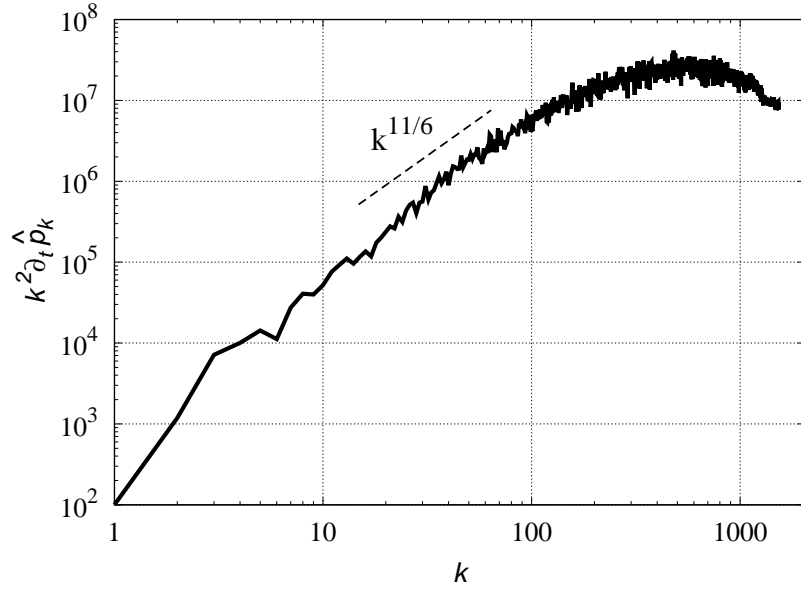


FIG. 8. Spectrum of the temporal derivative of the pressure field rescaled by k^2 . Results correspond to the forced HIT simulation at $Re_\lambda \approx 433$ from the JHTDB database^{24,25}

leading to the following spectra relation and power-law scaling

$$k^2 \partial_t \hat{p}_k \approx 2 \partial_t \hat{Q}_G \quad \stackrel{(13)}{\Rightarrow} \quad k^2 \partial_t \hat{p}_k \propto k^\beta \quad \text{with} \quad \beta = 11/6 \quad (\text{for NS}). \quad (42)$$

Nevertheless, this would still require computing a shell-summed spectrum of $\partial_t p$, which is not feasible for non-homogeneous flows. Instead, we can analyze the corresponding temporal spectra and invoke Taylor's frozen-flow hypothesis⁵⁴ to relate them to the spectral distribution of the spatial scales. To demonstrate the validity of this approach, Figure 8 presents the analysis for the HIT case discussed in the previous subsection. For this dataset, a sequence of 5028 consecutive frames, stored every ten time-steps of the DNS simulation, was available. To improve statistical convergence, the temporal evolution of pressure was extracted at eight evenly spaced locations, their individual spectra were computed, and the results were subsequently averaged. The figure clearly shows the expected 11/6 scaling, thereby validating the proposed approach.

At this stage, we used the same analysis for the two above-mentioned configurations. Figures 9 and 10 show results for the flow around a square cylinder at $Re = 22000$ and $Re = 55000$, respectively. For the first case, the numerical setup, including the mesh, discretization schemes, and boundary conditions, was the same as in the original study¹⁶. The grid resolution in this case was $1272 \times 1174 \times 216$ in the stream-wise, cross-stream and span-

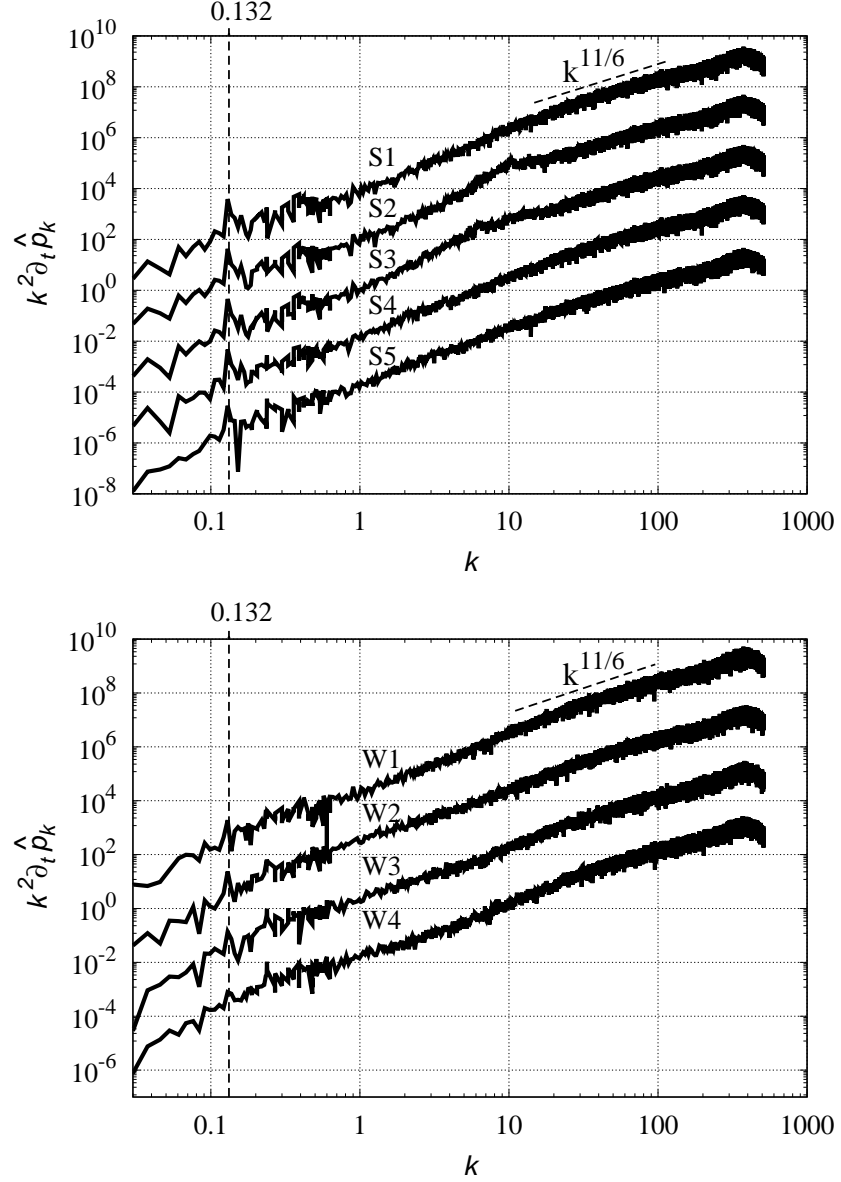


FIG. 9. Spectra of the temporal derivative of the pressure field rescaled by k^2 . Results correspond to the turbulent flow around a square cylinder at $Re = 22000$ displayed in Figure 7 (bottom). Top: results for a set of points located in the shear layer. Bottom: results for a set of points located in the wake regions. See Table II, for details.

wise direction, respectively, corresponding to approximately 323 million grid points. For the higher Reynolds number, the configuration was kept identical except for the use of a finer mesh of $2544 \times 2348 \times 432 \approx 2.6$ billion grid points. For both Reynolds numbers, the time evolution of the pressure was analyzed at the monitoring locations listed in Table II. The

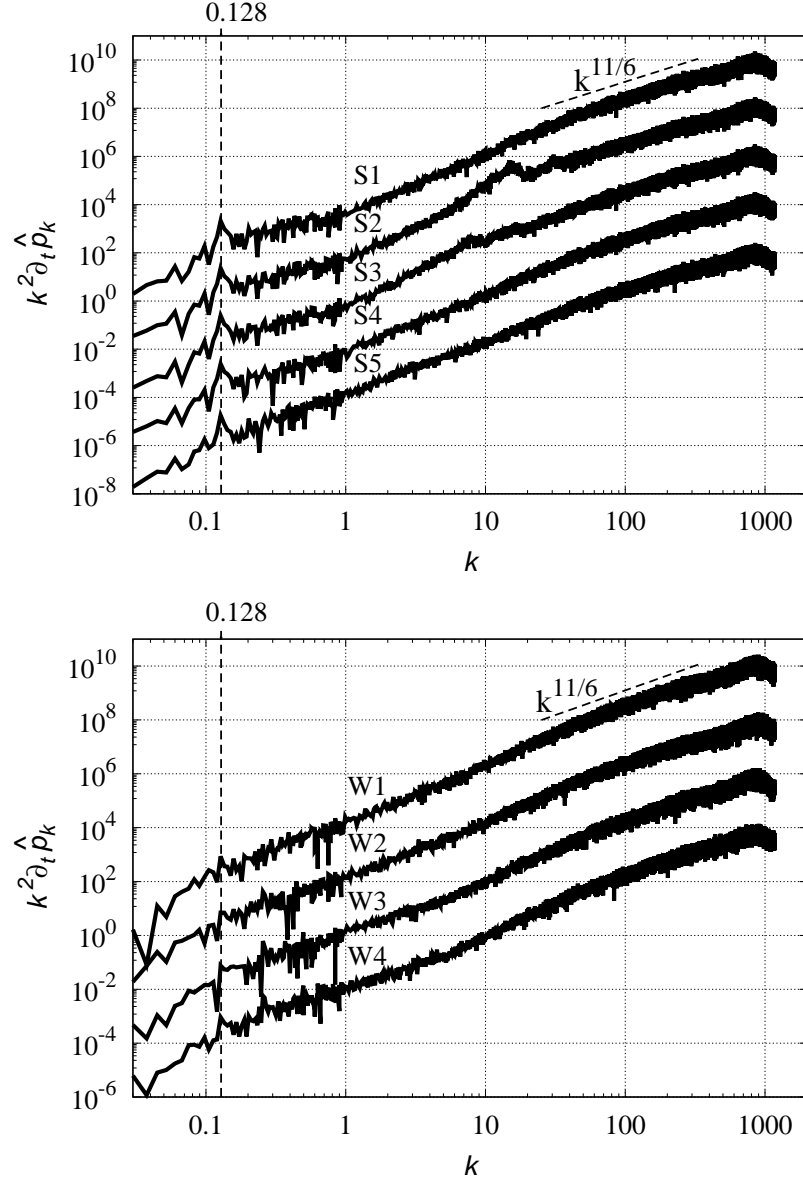


FIG. 10. Same as Figure 9, but for $Re = 55000$.

first five probes, labeled S1-S5, are located in the shear-layer region, while the remaining probes, labeled W1-W4, are located in the wake region. The same set of probes were used in our previous study¹⁶ for characterizing the onset and development of instabilities. The first five probes are placed near the upper corner of the cylinder, where small vortices generated by the Kelvin–Helmholtz instabilities rapidly develop and are convected downstream. These structures are clearly visible in the instantaneous snapshot of Figure 7 (see also the corresponding movie). As they evolve, the vortices grow in size and trigger the transition

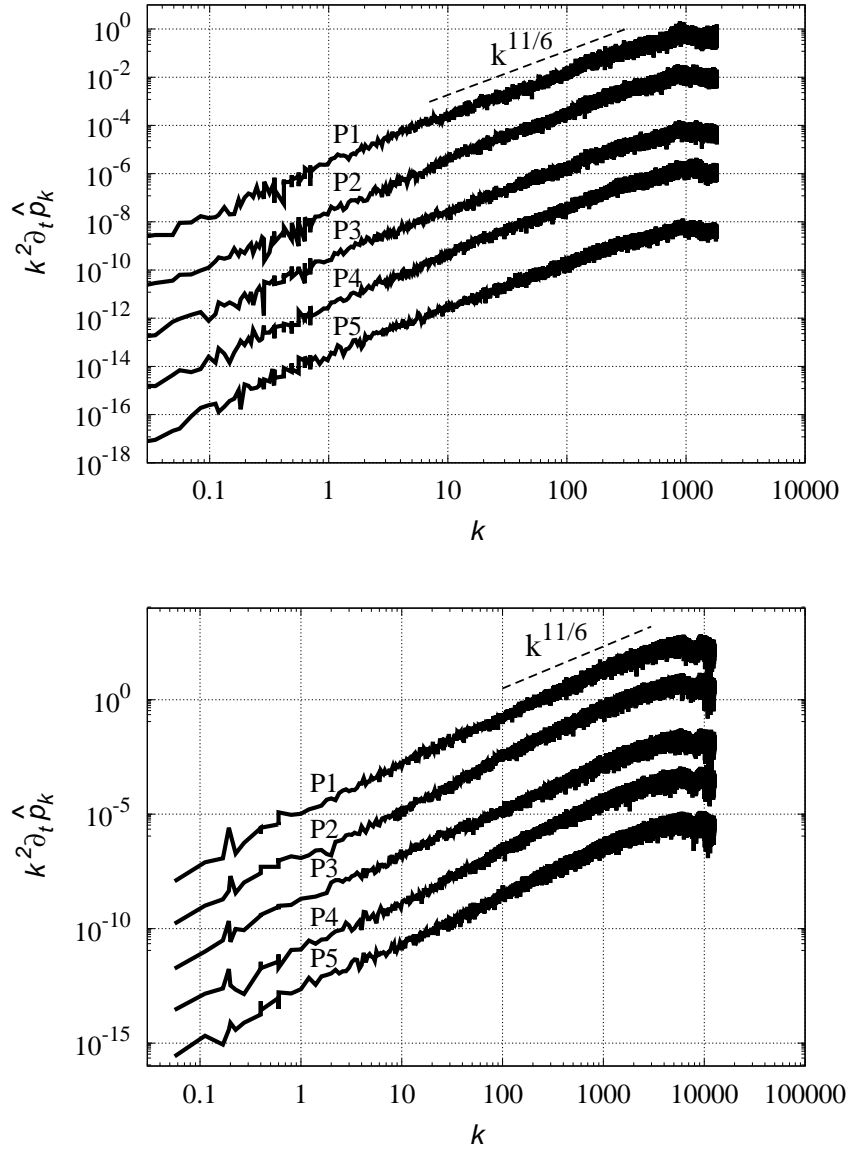


FIG. 11. Spectra of the temporal derivative of the pressure field rescaled by k^2 . Results correspond to the air-filled Raleigh–Bénard convection flow at $Ra = 10^{10}$ (top) and 10^{11} (bottom) displayed in Figure 7 (top). See Table III, for details.

to turbulence before reaching the downstream edge of the cylinder. They eventually break up into finer scales and are entrained by the much larger von Kármán vortices. The first Kelvin–Helmholtz structure appears at $x \approx -0.45$ (point S1), in very good agreement with previous experimental⁶³ and numerical studies¹⁶. However, the dominant frequency in both the shear-layer and wake regions corresponds to the von Kármán mode, taking values of

0.132 for $Re = 22000$ (see Figure 9) and 0.128 at $Re = 55000$ (see Figure 10), respectively. These results are in excellent agreement with previous experimental observations and confirm the very weak Re -number dependence of the Strouhal number in this range of Re -numbers⁶⁴. Nevertheless, the most significant feature observed in Figures 9 and 10 is the predicted $\beta = 11/6$ scaling at high wavenumbers, thereby confirming this power-law behavior for non-homogeneous flows across different Reynolds numbers.

As a second test-case for non-homogeneous flows, we consider an air-filled ($Pr = 0.7$) RBC at $Ra = 10^{10}$ and 10^{11} . These cases were already investigated in a previous study¹³, where the flow topology and its main features were analyzed in detail. Again, the numerical setup, including the mesh, discretization schemes, and boundary conditions, is the same as in the previous papers^{13,65}. The mesh resolution is $1024 \times 768 \times 768 \approx 604$ million grid points for $Ra = 10^{10}$, and $2048 \times 1662 \times 1662 \approx 5.7$ billion grid points in the homogeneous spanwise direction, the horizontal cross stream direction and the vertical direction, respectively. The flow exhibits strong inhomogeneity in the vertical direction, with thin thermal and velocity boundary layers adjacent to the horizontal isothermal plates and a plume-dominated bulk region. To capture these distinct flow regions, five monitoring points are considered in the analysis: namely, probes P1 and P2 are located inside the boundary layer whereas probes P3 to P5 are in the bulk region (see Table III, for details). Despite such complexity, the spectra of $k^2 \partial_t p$ showed in Figure 11 display very similar trends to those observed for the square cylinder. Namely, both cases clearly show the predicted $\beta = 11/6$ slope at high wavenumbers, thereby confirming that the theoretical scaling extends robustly to buoyancy-driven turbulence at very high Rayleigh numbers.

The consistent results obtained for both the square cylinder and the RBC at different Re and Ra numbers provide strong additional support for the theoretical framework developed in this paper, demonstrating its validity beyond the homogeneous case. They also indicate that the solver convergence trends inferred from the theory remain applicable in realistic CFD settings, where non-homogeneity and geometric complexity are unavoidable. Nevertheless, the predicted scaling of the number of solver iterations with respect to Re (see Eq. 32) still needs to be tested over a broader range of Reynolds numbers. This issue is addressed in the following subsection.

C. Towards very high Reynolds numbers

To further assess the validity of the theoretical framework at very high Reynolds numbers, we consider the Burgers' equation in a periodic one-dimensional domain as a simplified model problem,

$$\frac{\partial u}{\partial t} + u \frac{\partial u}{\partial x} = \frac{1}{Re} \frac{\partial^2 u}{\partial x^2} + f. \quad (43)$$

The equation is solved using a pseudo-spectral approach with the standard 3/2 dealiasing rule applied to the non-linear convective term. The forcing term, f , acts only at the smallest wavenumber, $k = 1$, keeping its energy constant to unity, *i.e.* $E_1 = 1$. The simulations are advanced in time until a statistically steady state is reached. Once convergence is achieved, the resulting velocity field is projected onto the space of divergence-free functions, which in this simplified setting reduces to solving a one-dimensional Poisson equation by means of either a Jacobi iterative solver or a MG solver using Jacobi as smoother at each level. The analysis covers a very wide range of Re -numbers from $Re = 2^5 = 32$ up to $Re = 2^{21} \approx 2.1M$. They are solved with $N = 4Re$ Fourier modes, *i.e.* from $N = 2^7 = 128$ up to $N = 2^{23} \approx 8.4M$. This linear resolution criterion arise from the fact that, according to the classical Cole–Hopf transformation^{66,67}, the smallest dissipative scale in the 1D Burgers' equation is inversely proportional to the Reynolds number. The adopted resolution is, in practice, very similar to that recommended in recent studies⁶⁸. Hence, for the 1D Burgers' equation, $\Delta x \sim lRe^{-1}$, where l is the characteristic length scale of the largest flow structures. Then, following the same arguments as in Eqs.(5) and (6), it leads to

$$\frac{\Delta t}{t_l} \sim \frac{1}{N_t} \sim Re^\alpha \quad \text{with} \quad \alpha = -1 \quad (\text{for Burgers' equation}), \quad (44)$$

which is the counterpart of Eq.(7). Notice that, in this case, the Reynolds-number scaling is the same whether the CFL stability constraint (see Eq. 4) is limited by convection or by diffusion.

Apart from this, the theoretical arguments developed in Section II have to be adapted to the scaling properties of the Burgers' equation (see Table I). Namely, in this case, the slope for the solver's residual is $\beta = 3$. This follows for the well-known k^{-2} energy spectrum⁶⁹, which can be clearly observed in the spectra shown in Figure 12. Namely, applying the same

arguments used in Section II B, it leads to the following relation for the residual

$$r^0 \approx \Delta t^q \partial_t \partial_x (u \partial_x u) \quad \text{with} \quad q = \begin{cases} 1 & \text{if } r^0 \text{ defined as in Eq.(9)} \\ 2 & \text{if } r^0 \text{ defined as in Eq.(10)} \end{cases} \quad (45)$$

which is the counterpart of Eq.(12). Then, we can easily relate the k^{-2} scaling in kinetic energy with the scaling of the convective term, $u \partial_x u$, using the equilibrium hypothesis (see Eq. 20),

$$(\widehat{u \partial_x u})_k \sim \frac{k^2}{Re} \hat{u}_k \propto k^2 k^{-1} = k. \quad (46)$$

Finally, following the same line of arguments as in Eqs.(16) and (19) leads to

$$\hat{r}_k^0 \propto Re^{-1} \Delta t^q k^\beta \quad \text{with} \quad \beta = 3 \quad \text{and} \quad q = \begin{cases} 1 & \text{if } \hat{r} \text{ defined as in Eq.(9)} \\ 2 & \text{if } \hat{r} \text{ defined as in Eq.(10)} \end{cases} \quad (47)$$

which is the counterpart of Eq.(21).

Results shown in Figure 13 (left) support the predicted k^3 scaling of the initial residual, \hat{r}_k^0 . Moreover, the compensated spectra in Figure 13 (right) demonstrate that all curves collapse irrespective of the Reynolds number, confirming the validity of the scaling law given in Eq. (47). In this particular case, $q = 2$, corresponds to the definition of the residual in Eq. (10), and $\Delta t \sim Re^{-1}$ as given in Eq. (44), which together yield the overall Re^{-3} dependence observed in Figure 13. Note that the discrepancies at very low wavenumbers in Figure 13 (right) arise from the amplification introduced by the k^{-3} scaling factor.

The final analysis shown in Figure 14 focuses on the dependence of the solver iteration count on the Reynolds number. As discussed above, the Poisson equation is solved using both a Jacobi solver and a MG solver employing Jacobi as a smoother at each level. The latter corresponds to the analysis done in Section III A. In all cases, the convergence criterion is set to $\|r\| \leq 10^{-6}$. Results obtained within this wide range of Reynolds numbers using the Jacobi solver are displayed in Figure 14 (top). They exhibit excellent agreement with the predicted scalings (see the last column of Table I), namely $\xi = 2/7$ for $q = 2$ and $\xi = 6/7$ for $q = 1$. This confirms that the proposed framework remains valid not only for canonical turbulent flows such as HIT, RBC, or bluff-body wakes, but also for this simplified model at very high Reynolds numbers. Furthermore, results obtained with the Jacobi solver for $q = 2$ are compared with the MG solver considering two scenarios: (i) fixing the size of the coarsest MG level to $N_{\text{low}} = 2^5 = 32$ modes, *i.e.* $l_{\text{max}} = (\log_2 N - 1)/5$, and (ii) using

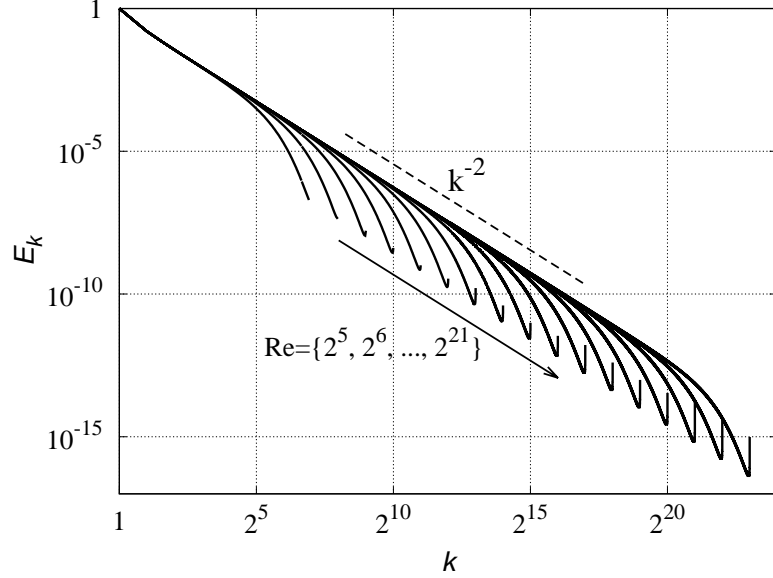


FIG. 12. Energy spectra for the forced Burgers' equation for $Re = \{2^5, 2^6, \dots, 2^{21}\}$, which have been numerically solved using $N = \{2^7, 2^8, \dots, 2^{23}\}$ Fourier modes.

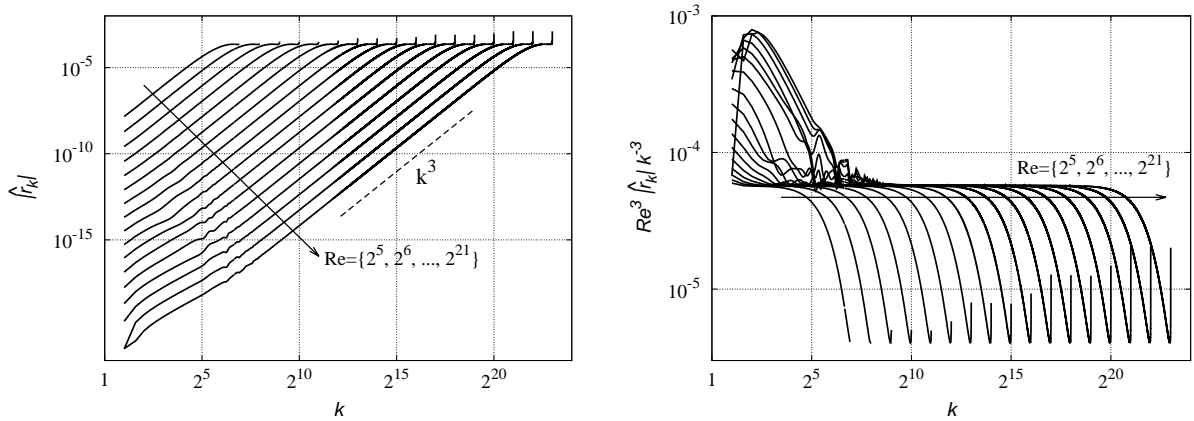


FIG. 13. Same as in Figure 12, but for the residual of the Poisson equation (left) and its compensated spectra (right).

the same configuration but limiting $l_{\max} \leq 2$, *i.e.* $l_{\max} = \min(\log_2 N - 1)/5, 2$. Thus, both configurations coincide for small N , whereas for large values of N , the latter recovers the $\xi = 2/7$ scaling.

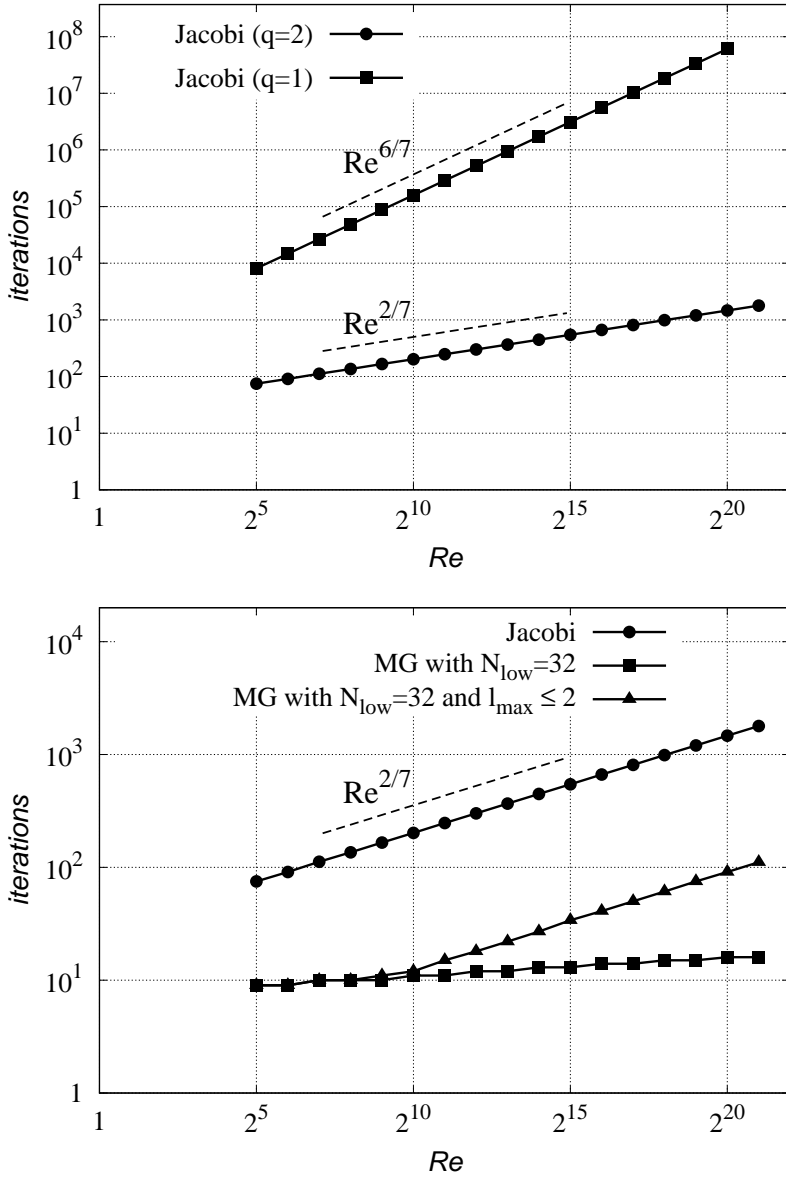


FIG. 14. Same as in Figure 12, but for the total number of iterations required to solve the Poisson equation for different solver options. Top: Jacobi solver with $q = \{1, 2\}$. Bottom: comparison between Jacobi and MG solver with $q = 2$.

V. CONCLUDING REMARKS

In this work, we have combined physical reasoning and numerical analysis to examine how the computational cost of solving the pressure Poisson equation evolves with increasing Reynolds number in simulations of incompressible flows. By analyzing the spectral distribution of the solver residual, two competing mechanisms were identified: the reduction of the

time step at higher Reynolds numbers, which improves the quality of the initial guess, and the refinement of the computational mesh, which worsens the conditioning of the discrete operator. The balance between these effects determines whether the convergence of the solver accelerates or deteriorates as Re -number increases.

For NS turbulence, our theoretical analysis predicts that the beneficial effect of smaller time steps dominates. Consequently, the number of iterations required by standard iterative solvers tends to decrease with increasing Re -numbers. The predicted residual scalings have been confirmed for all turbulent configurations considered, *i.e.* homogeneous isotropic turbulence, Rayleigh–Bénard convection, and bluff-body wakes, supporting the validity of the proposed framework. In contrast, for the one-dimensional Burgers’ equation, the cost of solving the Poisson equation increases with Re . This simplified model allows simulations over a much broader range of Reynolds numbers, providing an extensive validation of the theoretical scaling laws derived here.

Overall, these findings indicate that, although the Poisson equation remains the main bottleneck in incompressible CFD, its relative computational cost may lessen for very high Re -numbers. The proposed theoretical framework thus provides a unified perspective on how solver performance scales with Re -number and offers valuable guidance for the development of next-generation preconditioning and MG strategies for extreme-scale CFD simulations.

ACKNOWLEDGMENTS

This work was financially supported by the SIMEX project (PID2022-142174OB-I00) of *Ministerio de Ciencia e Innovación* MCIN/AEI/ 10.13039/501100011033 and the European Union Next GenerationEU. A.A.B. was financially supported by the EU’s Horizon Europe programme under the Marie Skłodowska-Curie grant agreement No. 101208388. Views and opinions expressed are however those of the authors only and do not necessarily reflect those of the European Union or the European Research Executive Agency. Neither the European Union nor the granting authority can be held responsible for them. Calculations were carried out on the MareNostrum 5-GPP supercomputer at BSC. We thankfully acknowledge these institutions.

REFERENCES

¹J. H. Ferziger, M. Perić, and R. L. Street. *Computational Methods for Fluid Dynamics*. Springer, 4th edition, 2020.

²S. A. Orszag and G. S. Patterson. Numerical simulation of three-dimensional homogeneous isotropic turbulence. *Physical Review Letters*, 28:76–79, 1972.

³D. I. Pullin. Pressure spectra for vortex models of fine-scale homogeneous turbulence. *Physics of Fluids*, 7:849, 1995.

⁴N. Cao, S. Chen, and G. D. Doolen. Statistics and structures of pressure in isotropic turbulence. *Physics of Fluids*, 11(8):2235–2250, 1999.

⁵J. Kim, P. Moin, and R. Moser. Turbulence statistics in fully developed channel flow at low Reynolds number. *Journal of Fluid Mechanics*, 177:133–166, 1987.

⁶R. D. Moser, J. Kim, and N. N. Mansour. Direct numerical simulation of turbulent channel flow up to $Re_\tau = 590$. *Physics of Fluids*, 11:943–945, 1999.

⁷C. Canuto, M. Hussaini, A. Quarteroni, and T. Zang. *Spectral Methods in Fluid Dynamics*. Springer, Berlin, Heidelberg, 1988.

⁸Yukio Kaneda and Mitsuo Yokokawa. DNS of Canonical Turbulence with up to 4096^3 Grid Points. In *Parallel Computational Fluid Dynamics*, pages 23–32. Elsevier, May 2004.

⁹S. Hoyas and J. Jiménez. Scaling of velocity fluctuations in turbulent channels up to $Re_\tau = 2003$. *Physics of Fluids*, 18:011702, 2006.

¹⁰T. Ishihara, T. Gotoh, and Y. Kaneda. Study of high–Reynolds number isotropic turbulence by direct numerical simulation. *Annual Review of Fluid Mechanics*, 41:165–180, 2009.

¹¹R.J.A.M. Stevens, D. Lohse, and R. Verzicco. Prandtl and Rayleigh number dependence of heat transport in high Rayleigh number thermal convection. *Journal of Fluid Mechanics*, 688:31–43, 2011.

¹²M. Lee and R. D. Moser. Direct numerical simulation of turbulent channel flow up to $Re_\tau \approx 5200$. *Journal of Fluid Mechanics*, 774:395–415, 2015.

¹³F. Dabbagh, F. X. Trias, A. Gorobets, and A. Oliva. Flow topology dynamics in a three-dimensional phase space for turbulent Rayleigh–Bénard convection. *Physical Review Fluids*, 5:024603, 2020.

¹⁴S. Pirozzoli and T. Wei. On the near-wall behavior of pressure spectra in high-Reynolds-number wall turbulence. *Journal of Fluid Mechanics*, 1010:A10, 2025.

¹⁵R. Vinuesa, P. Schlatter, J. Malm, C. Mavriplis, and D. S. Henningson. Direct numerical simulation of the flow around a wall-mounted square cylinder under various inflow conditions. *Journal of Turbulence*, 16(6):555–587, 2015.

¹⁶F. X. Trias, A. Gorobets, and A. Oliva. Turbulent flow around a square cylinder at Reynolds number 22000: a DNS study. *Computers & Fluids*, 123:87–98, 2015.

¹⁷A. Pont-Vilchez, F. X. Trias, A. Gorobets, and A. Oliva. Direct Numerical Simulation of Backward-Facing Step flow at $Re_\tau = 395$ and expansion ratio 2. *Journal of Fluid Mechanics*, 863:341–363, 2019.

¹⁸J. S. Kern. Direct numerical simulations of an airfoil undergoing dynamic stall at different background disturbance levels. *Journal of Fluid Mechanics*, 986:A3(1–31), 2024.

¹⁹S. Park. Direct numerical simulation for backward-facing step flow with turbulence anisotropy analysis in a fully staggered curvilinear grid. *Physics of Fluids*, 36(9):095107, 2024.

²⁰D. V. Duong, L. V. Nguyen, D. V. Nguyen, T. C. Dinh, L. R. Zuhal, and L. I. Ngo. Direct numerical simulation of 45° oblique flow past surface-mounted square cylinder. *Journal of Fluid Mechanics*, 992:A12, 2024.

²¹W. Ling, Z. Wang, W. Huang, S. Gao, and G. Xi. Direct numerical simulation of flat-plate transition induced by spanwise adjacent roughness elements and inlet free-stream turbulence. *Physics of Fluids*, 37(3):034111, 2025.

²²W. Gao, M. Wang, and M. Parsani. Direct numerical simulation of particle-laden turbulent channel flow over superhydrophobic surfaces. *Physics of Fluids*, 37(3):035107, 2025.

²³M. Kouchakzad, A. Sohankar, and M. R. Rastan. Direct numerical simulation of flow around two non-identical tandem cylinders: study of secondary wake transition and flow structure. *Physics of Fluids*, 37(6):064112, 2025.

²⁴E. Perlman, R. Burns, Y. Li, and C. Meneveau. Data exploration of turbulence simulations using a database cluster. In *Proceedings of the ACM/IEEE Conference on Supercomputing (SC07)*, pages 1–11, 2007.

²⁵Y. Li, E. Perlman, M. Wan, Y. Yang, C. Meneveau, R. Burns, S. Chen, A. Szalay, and G. Eyink. Public turbulence databases for hydrodynamics research. In *Proceedings of the ACM/IEEE Conference on Supercomputing (SC08)*, pages 1–11, 2008.

²⁶J. B. Perot. Discrete conservation properties of unstructured mesh schemes. *Annual Review of Fluid Mechanics*, 43:299–318, 2011.

²⁷B. Koren, R. Abgrall, P. Bochev, J. Frank, and B. Perot. Physics-compatible numerical methods. *Journal of Computational Physics*, 257:1039, 2014.

²⁸F. X. Trias, O. Lehmkuhl, A. Oliva, C.D. Pérez-Segarra, and R.W.C.P. Verstappen. Symmetry-preserving discretization of Navier-Stokes equations on collocated unstructured meshes. *Journal of Computational Physics*, 258:246–267, 2014.

²⁹E. M. J. Komen, L. H. Camilo, A. Shams, B. J. Geurts, and B. Koren. A quantification method for numerical dissipation in quasi-DNS and under-resolved DNS, and effects of numerical dissipation in quasi-DNS and under-resolved DNS of turbulent channel flows. *Journal of Computational Physics*, 345:565–595, 2017.

³⁰N. Valle, F. X. Trias, and J. Castro. An energy-preserving level set method for multiphase flows. *Journal of Computational Physics*, 400(1):108991, 2020.

³¹Y. Zhang, A. Palha, M. Gerritsma, and L. G. Rebholz. A mass-, kinetic energy- and helicity-conserving mimetic dual-field discretization for three-dimensional incompressible Navier-Stokes equations, part I: Periodic domains. *Journal of Computational Physics*, 451:110868, 2022.

³²G. Coppola and A. E. P. Veldman. Global and local conservation of mass, momentum and kinetic energy in the simulation of compressible flow. *Journal of Computational Physics*, 475:111879, 2023.

³³A. J. Chorin. Numerical Solution of the Navier-Stokes Equations. *Mathematics of Computation*, 22:745–762, 1968.

³⁴F. X. Trias, X. Álvarez-Farré, À. Alsalti-Baldellou, A. Gorobets, and A. Oliva. An efficient eigenvalue bounding method: CFL condition revisited. *Computer Physics Communications*, 305:109351, 2024.

³⁵R. Courant, K. Friedrichs, and H. Lewy. Über die partiellen Differenzengleichungen der mathematischen Physik. *Mathematische Annalen*, 100(1):32–74, 1928.

³⁶Yousef Saad. *Iterative Methods for Sparse Linear Systems*. SIAM, second edition, 2003.

³⁷Michele Benzi. Preconditioning Techniques for Large Linear Systems: A Survey. *Journal of Computational Physics*, 182:418–477, 2002.

³⁸van der Vorst HA Meijerink JA. An iterative solution method for linear systems of which the coefficient matrix is a symmetric m-matrix. *Journal of Mathematical Computing*,

(31):148–162, 1977.

³⁹L Yu Kolotilina and A Yu Yeremin. Factorized sparse approximate inverse preconditionings I. Theory. *SIAM Journal on Matrix Analysis with applications*, 14(1):45 – 58, 08 1993.

⁴⁰G. Isotton, C. Janna, and M. Bernaschi. A GPU-accelerated adaptive FSAI preconditioner for massively parallel simulations. *The International Journal of High Performance Computing Applications*, 36(2):153–166, 2022.

⁴¹Klaus Stüben. An introduction to algebraic multigrid. In Ulrich Trottenberg, Cornelis Oosterlee, and Anton Schüller, editors, *Multigrid*, pages 413–532. Elsevier Academic Press, London, 2001.

⁴²Jinchao Xu and Ludmil Zikatanov. Algebraic Multigrid Methods. *Acta Numerica*, pages 1 – 127, 01 2017.

⁴³Uriel Frisch. *Turbulence. The Legacy of A.N.Kolmogorov*. Cambridge University Press, 1995.

⁴⁴A. Gorobets, F. X. Trias, M. Soria, and A. Oliva. A scalable parallel Poisson solver for three-dimensional problems with one periodic direction. *Computers & Fluids*, 39:525–538, 2010.

⁴⁵M. S. Dodd and A. Ferrante. A fast pressure-correction method for incompressible two-fluid flows. *Journal of Computational Physics*, 273:416–434, 2014.

⁴⁶P. Costa. A FFT-based finite-difference solver for massively-parallel direct numerical simulations of turbulent flows. *Computers & Mathematics with Applications*, 76(8):1853–1862, 2018.

⁴⁷G. K. Batchelor. Pressure fluctuations in isotropic turbulence. *Mathematical Proceedings of the Cambridge Philosophical Society*, 47:359–374, 1951.

⁴⁸Stephen B. Pope. *Turbulent Flows*. Cambridge University Press, 2000.

⁴⁹T. Gotoh and R. S. Rogallo. Intermittency and scaling of pressure at small scales in forced isotropic turbulence. *Journal of Fluid Mechanics*, 396:257–285, 1999.

⁵⁰T. Gotoh and D. Fukayama. Pressure spectrum in homogeneous turbulence. *Physical Review Letters*, 86:3775–3778, 2001.

⁵¹S. Zhao, E. Cheng, X. Qiu, I. Burnett, and J. Chia-chun Liu. Pressure spectra in turbulent flows in the inertial and the dissipation ranges. *The Journal of the Acoustical Society of America*, 140:4178–4182, 2016.

⁵²H. H. A. Xu, A. Towneb, X. I. A. Yang, and I. Marusic. Pressure power spectrum in high-Reynolds number wall-bounded flows. *International Journal of Heat and Fluid Flow*, 84:108620, 2020.

⁵³B. J. Cantwell. Exact solution of a restricted Euler equation for the velocity gradient tensor. *Physics of Fluids A*, 4:782–793, 1992.

⁵⁴G. I. Taylor. The spectrum of turbulence. *Proceedings of the Royal Society of London*, 164(919):476–490, 1938.

⁵⁵A. A. Townsend. *The Structure of Turbulent Shear Flow*. Cambridge University Press, second edition, 1976.

⁵⁶Y. Tsuji, D. M. McLaughlin, P. H. Alfredsson, and A. V. Johansson. Pressure statistics and their scaling in high-Reynolds-number turbulent boundary layers. *Journal of Fluid Mechanics*, 585:1–40, 2007.

⁵⁷S. S. Patwardhan and O. N. Ramesh. Scaling of pressure spectrum in turbulent boundary layers. In *Journal of Physics: Conference Series*, volume 506, page 012011, 2014.

⁵⁸J. Bechlars and R. D. Sandberg. Evolution of the velocity gradient tensor invariant dynamics in a turbulent boundary layer. *Journal of Fluid Mechanics*, 815:223–242, 2017.

⁵⁹S. Yigit, J. Hasslberger, M. Klein, and N. Chakraborty. Near wall Prandtl number effects on velocity gradient invariants and flow topologies in turbulent Rayleigh-Bénard convection. *Nature Scientific Reports*, 10(1):14887, 2020.

⁶⁰William L. Briggs. *A Multigrid Tutorial*. SIAM, Society for Industrial and Applied Mathematics, 1987.

⁶¹Petr Vacek, Erin Carson, and Kirk M. Soodhalter. The effect of approximate coarsest-level solves on the convergence of multigrid v-cycle methods. *SIAM Journal on Scientific Computing*, 46:A2634–A2659, 8 2024.

⁶²Y. Li, E. Perlman, M. Wan, Y. Yang, C. Meneveau, R. Burns, S. Chen, A. Szalay, and G. Eyink. A public turbulence database cluster and applications to study Lagrangian evolution of velocity increments in turbulence. *Journal of Turbulence*, 9:N31, 2008.

⁶³C. Brun, S. Aubrun, T. Goossens, and Ph. Ravier. Coherent structures and their frequency signature in the separated shear layer on the sides of a square cylinder. *Flow, Turbulence and Combustion*, 81(1-2):97–114, 2008.

⁶⁴H. Bai and M. M. Alam. Dependence of square cylinder wake on Reynolds number. *Physics of Fluids*, 30(1):015102, 01 2018.

⁶⁵F. Dabbagh, F. X. Trias, A. Gorobets, and A. Oliva. On the evolution of flow topology in turbulent Rayleigh-Bénard convection. *Physics of Fluids*, 28:115105, 2016.

⁶⁶J. D. Cole. On a quasi-linear parabolic equation occurring in aerodynamics. *Quarterly of Applied Mathematics*, 9(3):225–236, 1951.

⁶⁷E. Hopf. The partial differential equation $u_t + u u_x = \mu u_{xx}$. *Communications on Pure and Applied Mathematics*, 3:201–230, 1950.

⁶⁸C. Luo, J. Fang, and L. Fang. Minimum scale and spatial resolution requirement for direct numerical simulations of compressible turbulence. *Journal of Computational Physics*, 534:114014, 2025.

⁶⁹S. Alam, P. K. Sahu, and M. K. Verma. Universal functions for Burgers turbulence. *Physical Review Fluids*, 7:074605, 2022.